Supplementary Information (SI) for Green Chemistry.

Supporting Information

Piezocatalytic oxidation of lignin-derived phenol to *p*-Benzoquinone: A sustainable route for green polymerization inhibitors

Xinlei Ma [a], Bo Zhang [a,*], Xin Huang [b], Qing Xu [c], Roger Ruan [d]

[a] *Key Laboratory of En1ergy Thermal Conversion and Control of Ministry of Education and School of Energy and Environment, Southeast University, Nanjing, Jiangsu 210096, China.*

[b] *CAS Key Laboratory of Urban Pollutant Conversion Department of Environmental Science and Engineering, University of Science & Technology of China, Hefei 230026, China.*

[c] *College of Ocean Engineering and Energy, Guangdong Ocean University, Zhanjiang, Guangdong 524000, China.*

[d] *Center for Biorefining and Department of Bioproducts and Biosystems Engineering, University of Minnesota, St. Paul, MN 55108, USA.*

Corresponding author:

bozhang@seu.edu.cn (B. Zhang)

1.Experimental

1.1. Materials and reagents

Phenol (C_6H_6O, ≥ 99.0%), *p*-Benzoquinone ($C_6H_4O_2$, ≥ 99.0%), sodium sulfate (Na_2SO_4, 99.0%), sodium hydroxide (NaOH, ≥ 95.0%), ethanol (C_2H_6O, ≥ 99.5%), sulfuric acid (H_2SO_4, 98.0%), isopropyl alcohol (IPA, AR, ≥ 99.7%), ethylenediaminetetraacetic acid disodium salt (EDTA-2Na, ≥ 99.0%), superoxide dismutase (SOD, ≥ 7500 U/mg protein; Source: Bovine erythrocytes), L-histidine ($C_6H_9N_3O_2$, ≥ 99%), monopotassium phosphate (KH_2PO_4, ≥99.5%), terephthalic acid ($C_8H_6O_4$, ≥ 99%), and nitrotetrazolium blue chloride ($C_{40}H_{30}N_{10}O_6 \cdot 2Cl$, ≥ 98%), methanol ($CH_4O$, HPLC grade, 99.9%), formic acid (HCOOH, HPLC grade, 99.9%) were purchased from Aladdin Industrial Corporation (Shanghai, China), silver nitrate (AgNO3, 99.8%) was obtained from Nanjing Wanqing Chemical Glass & Instrument Co., Ltd. Nafion solution (5 wt.%) was procured from Alfa Aesar Chemical Co., Ltd. Nitrogen gas (N_2, 99.98%) was supplied by Nanjing Special Gas Factory Co., Ltd. Ultrapure water was used throughout the experiments, and all chemicals were of analytical grade.

1.2. Synthesis of catalysts

1T/2H-MoS_2（MIX）was prepared by the reported hydrothermal method [1]. Firstly, $Na_2MoO_4 \cdot 2H_2O$ and thiourea were dissolved in 90 mL of ultrapure water to form a homogeneous solution. Subsequently, the pH of the solution was adjusted to 1. Then the mixed solution was transferred into a Teflon-lined autoclave (100 mL) and heated at 200 °C for 18 h. Afterwards, the autoclave was cooled down to room temperature naturally and the resulted black precipitate in the autoclave was filtered and washed alternately with ultrapure water and ethanol. Finally, the collected products were dried in vacuum at 60 °C for future use.

1.3. Experimental procedure

Experimental Procedure for Nitrogen Atmosphere Control

A 30 mL aliquot of 0.2 mM phenol solution was transferred into a sealable reaction vessel equipped with gas inlet/outlet valves. The system was first evacuated using a vacuum pump and then refilled with high-purity nitrogen; this evacuation-refilling cycle was repeated three times to thoroughly remove residual air from the headspace. Subsequently, a continuous flow of nitrogen was bubbled through the solution for 30 minutes to purge dissolved oxygen. Under the protection of a nitrogen stream, 20 mg of the catalyst was added, and the system was sealed while maintaining a slight positive pressure of nitrogen throughout the entire ultrasonic reaction. The reaction was performed under otherwise identical conditions (40 kHz, 240W, 25 °C water bath) for 6 hours. After the reaction, the liquid sample was collected under the nitrogen atmosphere, filtered through a 0.22 μm membrane, and analyzed by HPLC. The control experiment in an air atmosphere was carried out in an open vessel without nitrogen purging, while all other conditions remained exactly the same [2].

Catalytic Performance under existing Impurities

A 0.2 mM phenol solution was used as the baseline system. Guaiacol and syringol were selected as the representative G-type and S-type model impurities, both of which are commonly found in lignin depolymerization bio-oils. These impurities were introduced at a molar ratio of 5% relative to phenol. The experimental groups were configured as follows: Group A served as the control (phenol only); Group B contained the G-type impurity (0.01 mM guaiacol + 0.19 mM phenol); Group C contained the S-type impurity (0.01 mM syringol + 0.19 mM phenol); and Group D contained mixed impurities (0.005 mM guaiacol + 0.005 mM syringol + 0.19 mM phenol). All groups were tested under identical conditions, with the same total liquid volume (30 mL) and catalyst dosage (20 mg of MS-3).

1.4. Characterizations

The morphologies of the synthesized piezocatalysts are analyzed using scanning electron microscopy (SEM, Sigma-360, Zeiss, Germany) and transmission electron microscopy (TEM, HRTEM, and SAED, JEM-F200, JEOL, Japan). SAED and Elemental mapping of the samples is performed with an energy dispersive spectrometer (JED-2300T, JEOL, Japan). The crystalline phase structures and heterojunction formation in the catalysts are analyzed using X-ray diffraction (XRD, XRD-6100, Shimadzu, Japan) and X-ray photoelectron spectroscopy (XPS, Nexsa, Thermo Fisher, USA). To assess the catalysts' energy band gaps, UV-visible diffuse reflectance spectra are recorded using a UV-vis spectrophotometer (752N, Shanghai Jingke Instrument Electric Co., Ltd, China). Piezoresponse force microscopy (PFM) analysis is carried out using an atomic force microscope (Dimension Icon, Bruker, Germany). Raman spectroscopy measurements were conducted on a Horiba LabRAM HR Evolution instrument. Steady-state and transient photoluminescence (PL) spectra were recorded using an Edinburgh Instruments FLS1000 spectrophotometer. Electron spin resonance (ESR) spectroscopy (BRUKER EMX, Bruker, USA) detects free radicals generated by the piezocatalysis through the use of 5,5-dimethyl-1-pyrroline-N-oxide (DMPO).

The concentration of generated H_2O_2 was quantified by an iodometric method, as follows. An aqueous solution (5 mL) of ammonium molybdate tetrahydrate ($H_{24}Mo_7N_6O_{24}\cdot 4H_2O$, 0.01 M) and a KI solution (10 mL, 0.1 M) were prepared. At different time intervals during the ultrasonic irradiation, 0.5 mL of the reaction solution was sampled and mixed with 2 mL of the KI solution and 50 μL of the ammonium molybdate solution. The resulting mixture was vigorously shaken and allowed to stand for 10 minutes before analysis by UV-Vis spectrophotometry at a maximum absorption wavelength of 351 nm.

The generation of $\cdot O_2^-$ and $\cdot OH$ radicals was detected using the nitroblue tetrazolium (NBT) transformation method and the terephthalic acid photoluminescence (TA-PL) probe method, respectively. NBT reacts with $\cdot O_2^-$ at a 1:4 molar ratio, enabling the quantitative detection of $\cdot O_2^-$ on the catalyst surface. The reaction was monitored by recording the absorbance changes via UV-Vis spectrophotometry. Conversely, terephthalic acid reacts with $\cdot OH$ in a 1:1 molar ratio to form 2-hydroxyterephthalic acid, which exhibits strong fluorescence at 425 nm under an excitation wavelength of 315 nm. The ·OH generation was thus quantified by measuring the corresponding PL intensity using a fluorescence spectrophotometer.

1.6. DFT calculations

All DFT computations in this work were carried out using the Vienna Ab initio Simulation Package (VASP) [3]. The Perdew–Burke–Ernzerhof (PBE) functional within the generalized gradient approximation (GGA) was employed to represent the exchange–correlation interactions [4]. The projector augmented wave (PAW) method was adopted to describe electron–ion interactions [5]. A plane-wave cutoff energy of 450 eV was applied, and Brillouin zone sampling was performed using a 2×2×1 Gamma-centered Monkhorst–Pack k-point grid. The self-consistent field iteration convergence was set at 10^{-5} eV for energy and 0.05 eV/Å for forces. To accurately model van der Waals (vdW) forces, the DFT-D3 correction scheme was incorporated [6]. The adsorption energy ($E_a$ds) was determined according to the equation:

$$E_a\mathrm{ds} = \mathrm{Etotal} - \mathrm{Eslab} - \mathrm{Eadsorbate}$$

where Etotal corresponds to the total energy of the adsorbed system, Eslab refers to the energy of the clean slab, and Eadsorbate denotes the energy of the isolated adsorbate molecule.

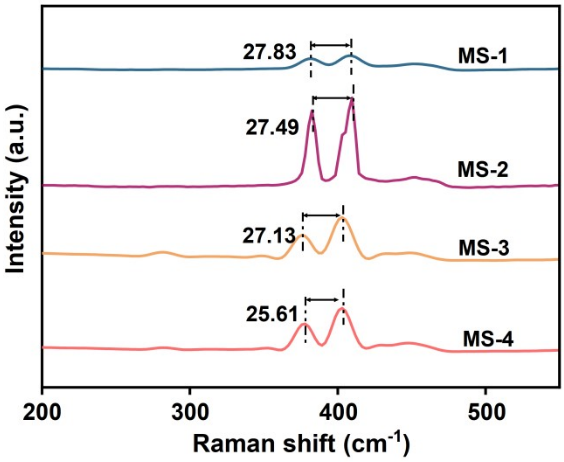

Fig.S1. Raman spectra of the MS-1, MS-2, MS-3 and MS-4 samples.

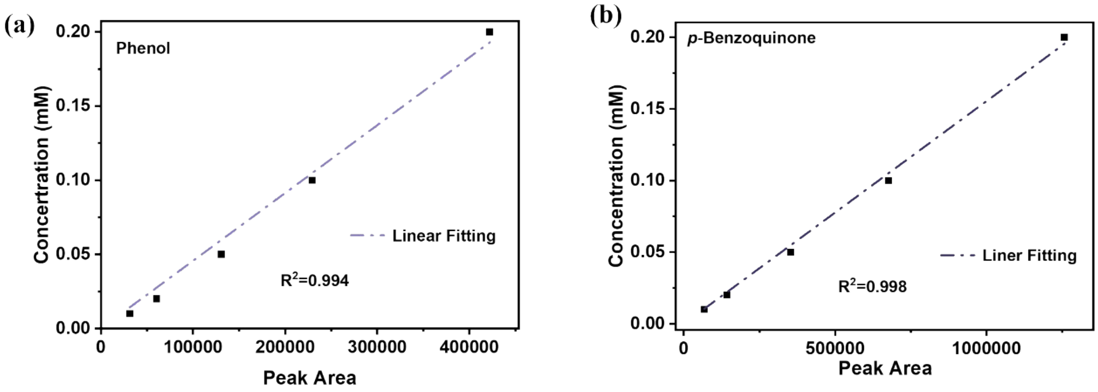

Fig. S2. The standard curves of phenol and *p*-Benzoquinone.

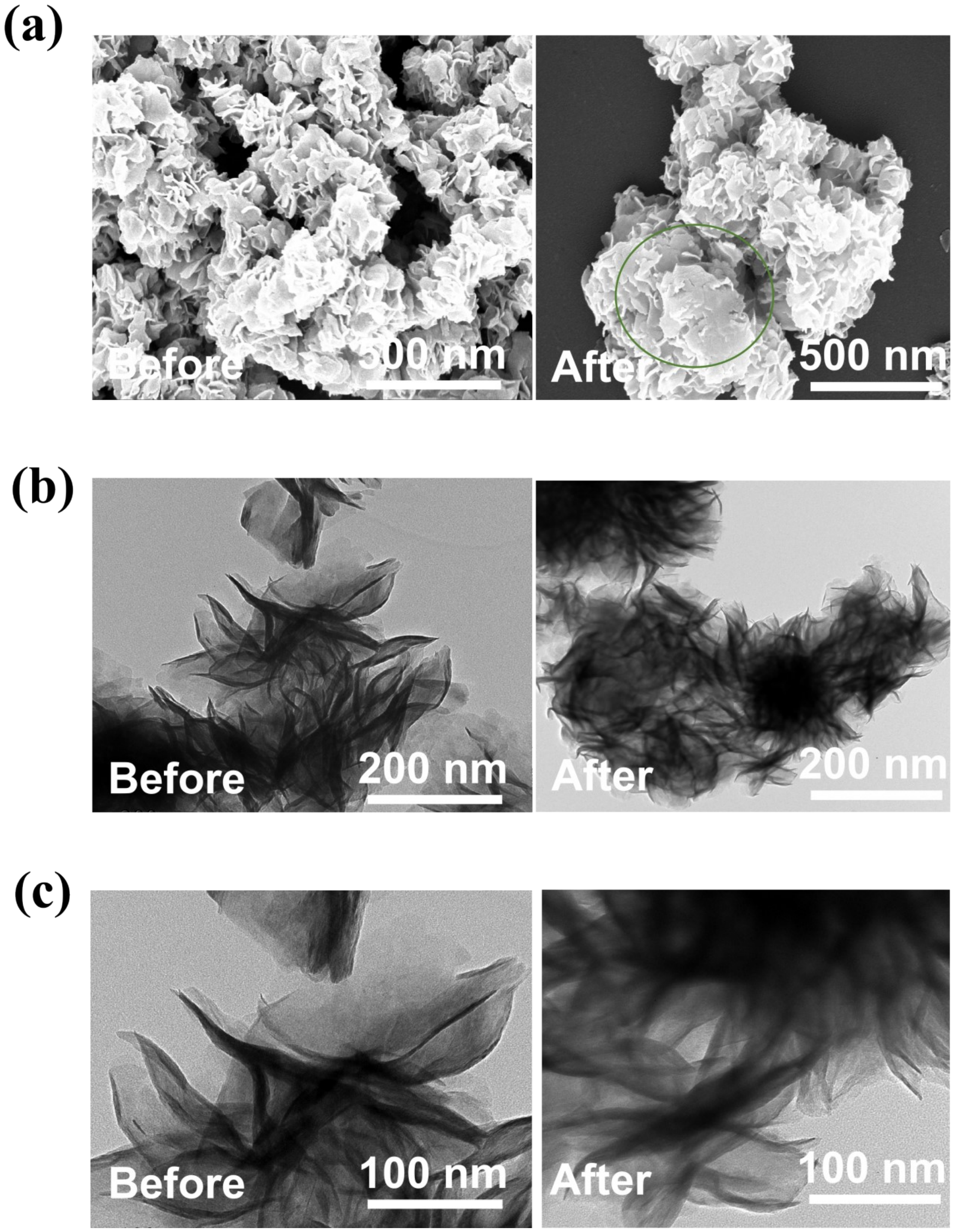

Fig. S3. SEM and TEM images of the catalyst MS-3 before and after the reaction.

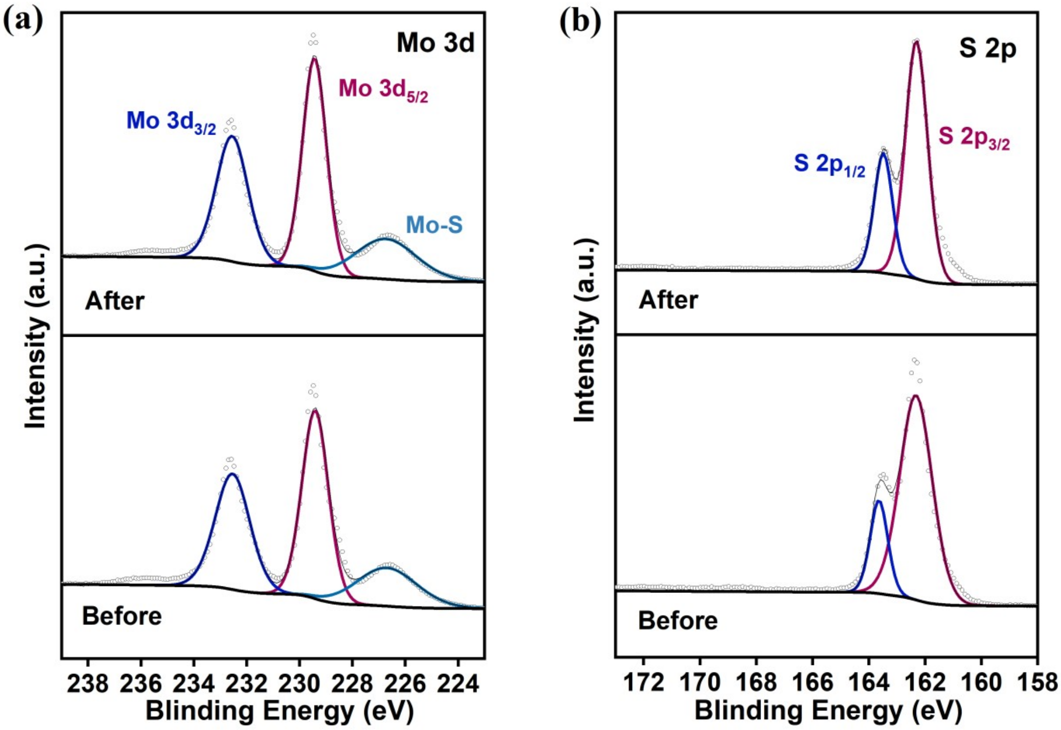

Fig. S4. High-resolution XPS spectra for (a) Mo 3d and (b) S 2p of MS-3 before and after cycling.

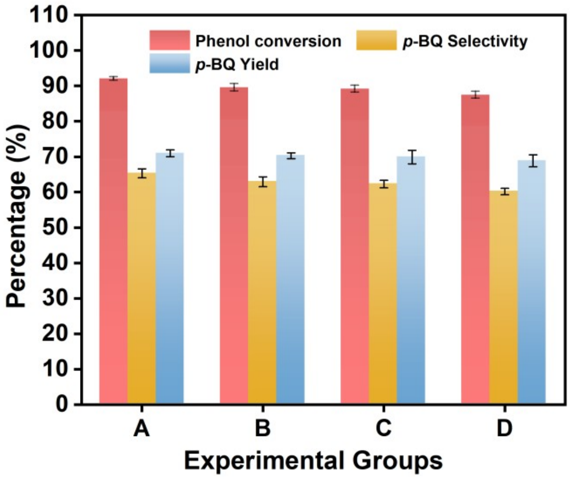

Fig. S5. Influence of impurities on the piezocatalytic performance of MS-3 for phenol oxidation to *p*-BQ. (A) Control (phenol only, 0.2 mM); (B) Phenol (0.19 mM) with guaiacol (0.01 mM); (C) Phenol (0.19 mM) with eugenol (0.01 mM); (D) Phenol (0.19 mM) with a mixture of guaiacol and eugenol (each 0.005 mM).

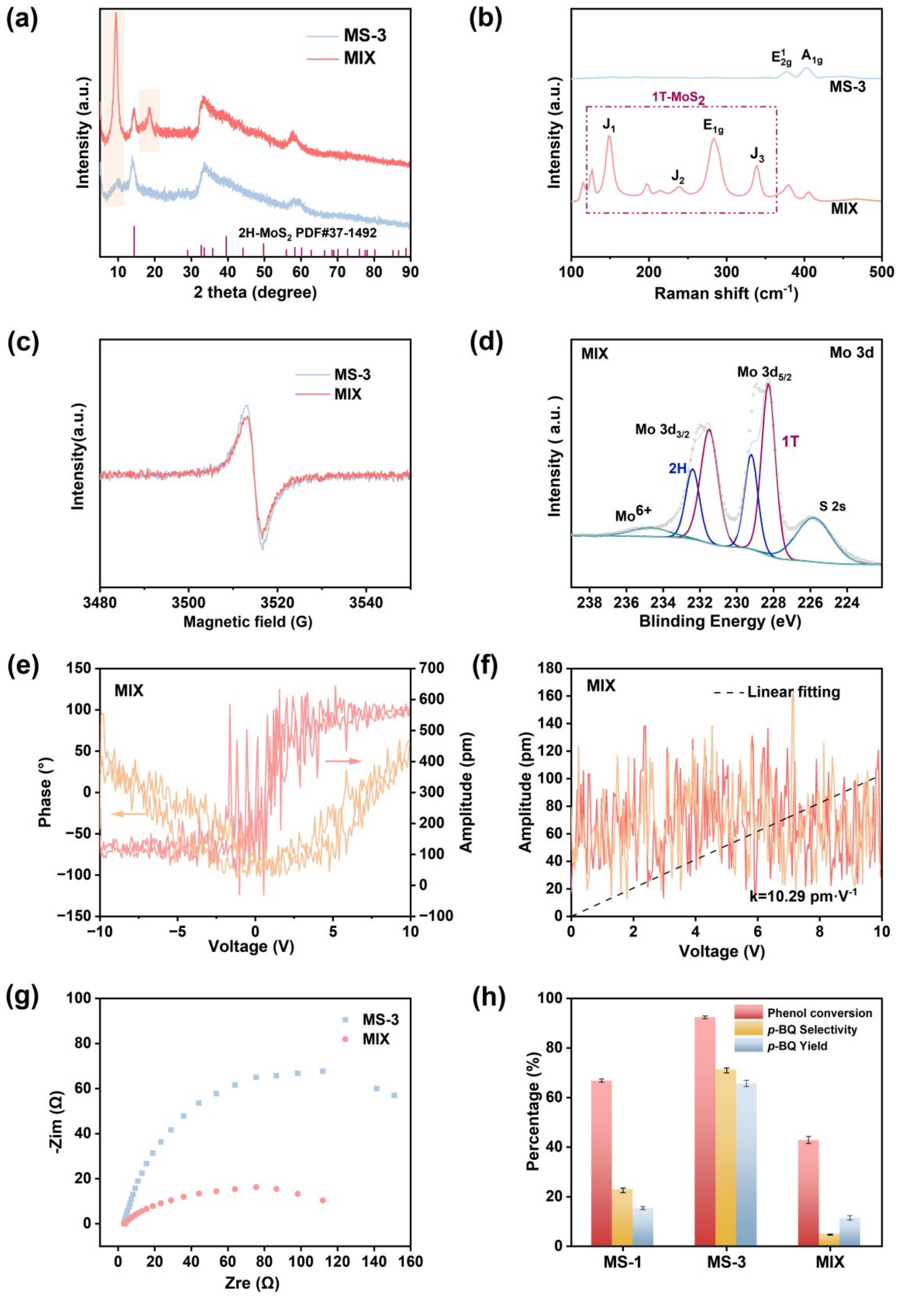

Fig. S6. (a) XRD patterns of MS-3 and MIX; (b) Raman spectra of MS-3 and MIX; (c) EPR measurements of sulfur vacancy concentrations in MS-3 and MIX; (d) High-resolution XPS spectrum of Mo 3d for MIX; PFM characterization of MIX: (e) Butterfly amplitude curve, (f) D_{33} coefficient curve; (g) EIS spectra of MS-3 and MIX; (h) Piezocatalytic performance of MS-3 and MIX for the conversion of phenol to *p*-BQ.

To further clarify the role of the 1T phase in the piezocatalytic conversion of phenol to *p*-BQ, a series of 1T/2H hybrid MoS_2 samples were synthesized via a hydrothermal method [1]. From this series, we selected a representative sample, designated as MIX, which featured a high 1T phase content while maintaining an S-vacancy concentration comparable to that of MS-3. The investigation proceeded by first confirming the phase composition of MIX, then assessing its piezoelectric performance, and comparing its electrochemical properties with MS-3. Finally, the piezocatalytic activity of MIX was systematically compared with that of MS-1 and MS-3, as shown in Fig. S6.

The XRD pattern (Fig. S6a) indicates that the diffraction peaks of MS-3 match perfectly with the standard card of 2H-MoS_2 (JCPDS No. 37-1492). In contrast, the MIX sample exhibits a notably enhanced characteristic diffraction peak around 9.8°, corresponding to the (002) plane of 1T-MoS_2 [7, 8]. Raman spectroscopy (Fig. S6b) reveals not only the characteristic E^1_2g and A_1g vibration modes of the 2H-MoS_2 phase, but also additional peaks at 147, 234, 284, and 336 cm^{-1}. These peaks are assigned to the J_1, J_2, E_1g, and J_3 vibrational modes of 1T-MoS_2, respectively [7, 9], providing further evidence for the presence of the 1T phase. Fig. S6c indicates that MIX has a sulfur vacancy concentration comparable to that of MS-3. Moreover, Mo 3d XPS analysis of

MIX (Fig. S6d) indicates that the Mo $3d_{3/2}$ and Mo $3d_{5/2}$ peaks can be deconvoluted into two doublets, attributed to the 2H and 1T phases. The characteristic peaks at 228.3 eV and 231.5 eV correspond to 1T-MoS_2, with binding energies approximately 0.95 eV lower than those of the 2H phase. The peak at 225.80 eV is associated with the Mo-S bond, while a minor Mo^{6+} signal likely arises from surface oxidation of partially unsaturated Mo atoms [10]. Quantitative fitting results show that the relative contents of the 1T and 2H phases derived from the Mo 3d spectrum are about 64.88% and 30.29%, respectively.

Given the centrosymmetric structure of the 1T phase, we further characterized the piezoelectric properties of MIX using piezoresponse force microscopy (PFM) and a D_{33} tester.As shown in Fig. S6e-f, MIX exhibits a weak piezoelectric response, with a noisy amplitude curve and a D_{33} coefficient of only 10.29 $pm\cdot V^{-1}$, which remains lower than that of MS-1. These results demonstrate that a high content of the 1T phase reduces the intrinsic piezoelectric response of the material. Electrochemical impedance spectroscopy (EIS) measurements (Fig. S6g) indicate that the Nyquist arc radius of MIX is smaller than that of MS-3, suggesting lower charge transfer resistance, consistent with the higher electrical conductivity of the 1T phase. In the piezocatalytic conversion of phenol to *p*-BQ (Fig. S6h), the catalytic activity of MIX is lower than that of the MS-series catalysts. After 6 hours of reaction, the phenol conversion, yield, and selectivity of MIX are 42.56%, 4.68%, and 11%, respectively. Thus, the inferior catalytic performance of MIX primarily originates from its weak piezoelectric response: although the 1T phase facilitates charge migration, its inherently low piezoelectric effect leads to insufficient polarization charge generation under external stress, limiting effective carrier separation and migration, and ultimately reducing piezocatalytic activity [2].

The systematic comparison of piezocatalytic performance and related mechanisms between MIX and MS-3 further demonstrates that the high-efficiency piezocatalytic conversion of phenol to *p*-BQ achieved in this study originates from the introduction of sulfur vacancies into the 2H-phase MoS_2 structure.

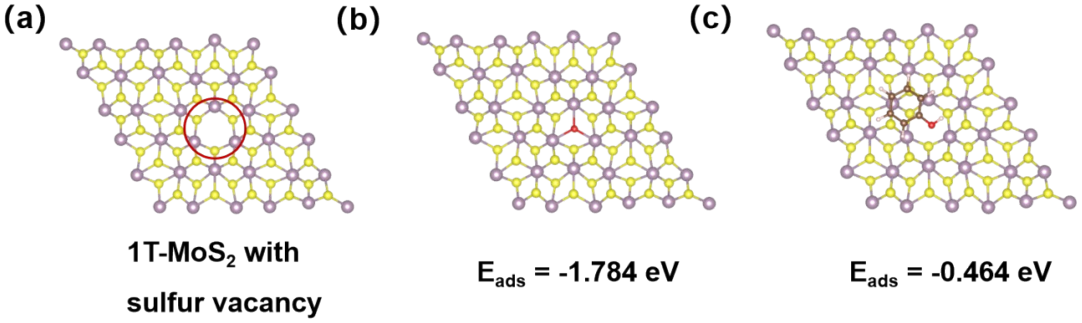

Fig. S7. DFT Calculations: (a) Theoretical model of 1T-MoS$_2$ with a sulfur vacancy. Adsorption energies of (b) oxygen (O$_2$) and (c) phenol on 1T-MoS$_2$ with a sulfur vacancy.

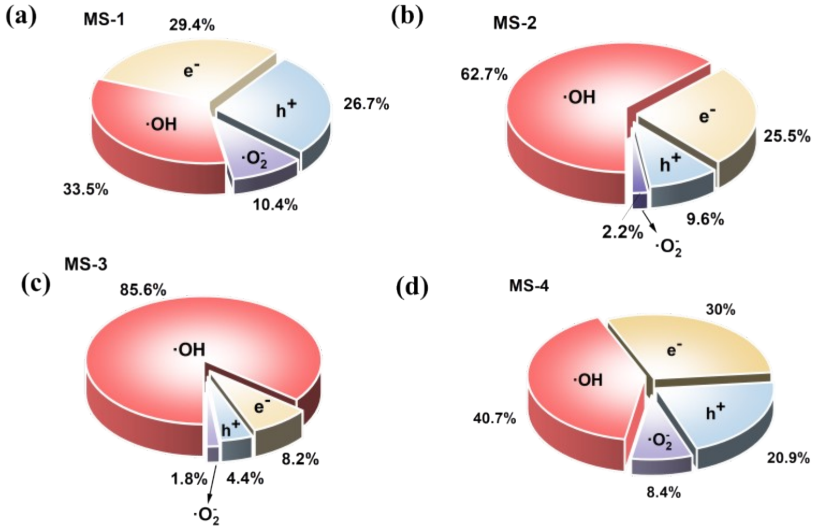

Fig. S8. Contributions of the four reactive species in (a) MS-1, (b) MS-2, (c) MS-3 and (d) MS-4.

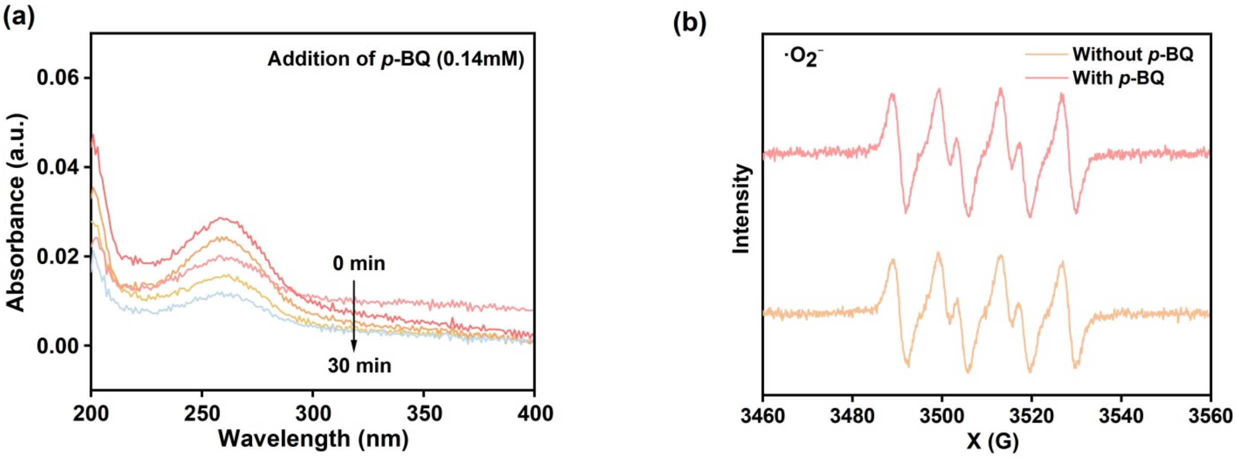

Fig. S9. (a) Probe experiment of superoxide radical after adding p-BQ; (b) EPR testing of superoxide radical with and without p-BQ addition.

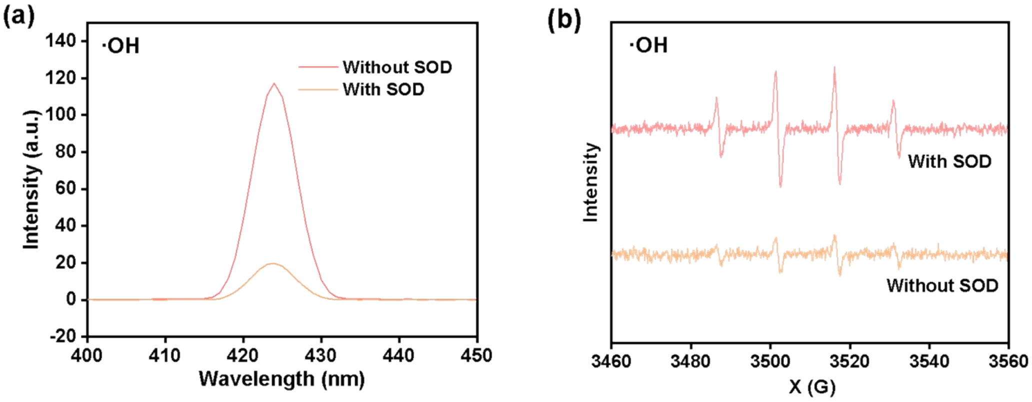

Fig. S10. (a) Probe experiment and (b) EPR analysis of hydroxyl radicals before and after adding superoxide dismutase (SOD).

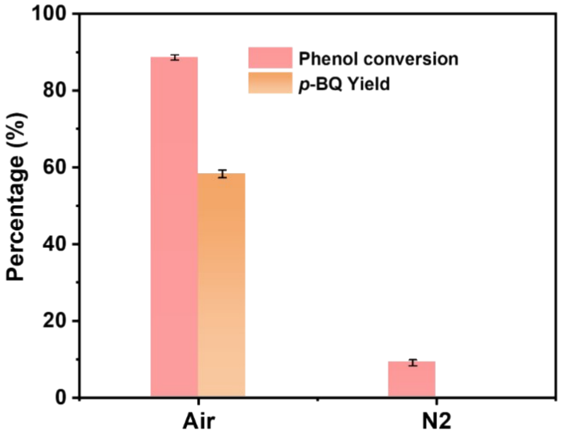

Fig. S11. Catalytic performance under different atmospheric conditions (Air and N_2).

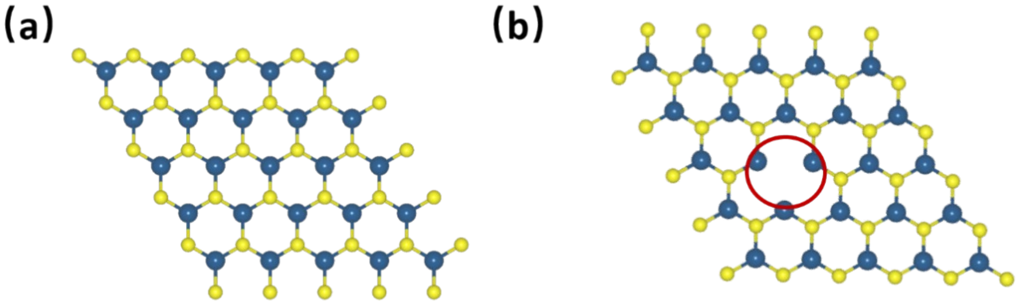

Fig. S12. Top View of the Optimized Models: (a) MoS_2 without sulfur vacancies; (b) MoS_2 with sulfur vacancies.

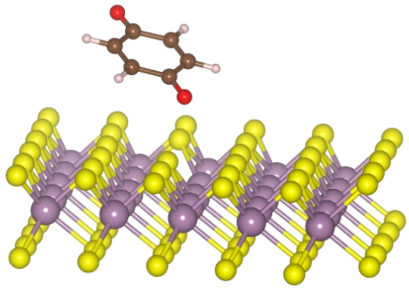

Eads = -0.553 eV

Fig. S13. The adsorption energy of *p*-BQ on MoS_2 with sulfur vacancies.

$$\alpha \cdot hv = \mathrm{A} \cdot (hv - Eg)^{n/2} \qquad \textbf{(4)}$$

Where α is the absorption coefficient, hv is the photon energy, A is the coefficient, and Eg is the energy band gap. n is related to the intrinsic properties of the semiconductor. MoS_2 is an direct semiconductor (n=1).

$$\mathrm{E\ (NHE) = E\ (Ag/AgCl) + 0.059 \times pH + E_0\ (Ag/AgCl)} \qquad \textbf{(5)}$$

Where E_0(Ag/AgCl) is approximately 0.197 V at 25°C.

$$E_{VB\text{-}NHE} = \Phi + 1.50\ \mathrm{eV} - 4.4 \qquad \textbf{(6)}$$

$E_{VB\text{-}NHE}$: VB potential versus the standard hydrogen electrode potential, Φ is 4.50 eV: the electron work function of the analyzer.

Table S1. The conversion of phenol to *p*-Benzoquinone was compared with other types of reactions

	Phenol conversion	***p*-Benzoquinone yield**	**Reaction conditions**	Ref.
1	95.8%	73.1%	pH = **7**	[11]
2	50 %	40 %	pH=3	[12]
3	\	64%	Catalyst: manganese or cobalt salts of p-aminobenzoic acid supported on silica gel.	[13]
4	\	66%	Solvent type: Acetonitrile.	[14]
5	48.3	48.2	Solvent type: 0.5 M H_2SO_4	[15]
7	48	73	Ethanol (5 mL) at 45°C, with H_2O_2 (35% aqueous solution)	[16]
8	92.57%	66.56%	MoS_2 with sulfur vacancies. Reaction conditions: in pure water without pH adjustment.	This work

Table S2. Adsorption energies of oxygen and phenol on pristine and S-vacancy 2H-MoS_2, and S-vacancy 1T-MoS_2 surfaces.

Adsorption Energy (eV)	Pristine 2H-MoS_2	2H-MoS2 with S-vacancy	1T-MoS2 with S-vacancy
O_2	-0.505	-2.323	-1.784
Phenol	-0.441	-0.615	-0.464

Reference

1. T. Jiang, C. Cai, H. Peng, J. Li, X. Fu, C. Nie and Z. Ao, Chemical Engineering Journal, 2025, 520, 165824.
2. X. Ning, A. Hao and X. Qiu, Advanced Functional Materials, 2025, 35, 2413217.
3. G. Kresse and J. Hafner, Physical Review B, 1994, 49, 14251–14269.
4. J. P. Perdew, K. Burke and M. Ernzerhof, Physical Review Letters, 1996, 77, 3865–3868.
5. G. Kresse and D. Joubert, Physical Review B, 1999, 59, 1758–1775.
6. S. Grimme, J. Antony, S. Ehrlich and H. Krieg, The Journal of Chemical Physics, 2010, 132, 154104.
7. H. Jin, Y. Zhang, Z. Cao, J. Liu and S. Ye, Advanced Materials, 2025, 37, 2502977.
8. S. Mondal, K. Dilly Rajan, L. Patra, M. Rathinam and V. Ganesh, Small, 2025, 21, 2411828.
9. H. Shi, Q. Li, Z. Xu, X. Zhang, Y. Ren, Q. Ma, F. Yu, M. Xu, L. Wang and J. Ma, Chemical Engineering Journal, 2025, 525, 170405.
10. X. Qi, Y. Zhu, Y. Xu, W. Chen, Z. Hu, L. Xi, Y. Xie, H. Hou, G. Zou and X. Ji, Energy Storage Materials, 2025, 75, 104063.
11. F. Liu, H. Dong, S. Zhong, X. Wu, T. Wang, X. Wang, Y. Liu, M. Zhu, I. M. C. Lo, S. Zhan and X. Guan, Water Research, 2024, 251, 121106.
12. D. Chillè, G. Papanikolaou, P. Squillaci, S. Abate, C. Cannilla, P. Lanzafame, S.

Perathoner and G. Centi, Applied Catalysis O: Open, 2025, 207, 207067.

13. M. M. Hashemi and Y. Ahmadi Beni, Journal of Chemical Research, Synopses, 1998, DOI: 10.1039/A705855A, 138–139.

14. Y. Wang, J. Liu, W. Sun, Y. Zhou, X. Wang, Q. Hu, Z. Wen, J. Yao and H. Li, The Journal of Organic Chemistry, 2024, 89, 2440–2447.

15. R. Wu, Q. Meng, J. Yan, H. Liu, Q. Zhu, L. Zheng, J. Zhang and B. Han, Journal of the American Chemical Society, 2022, 144, 1556–1571.

16. R. Saladino, V. Neri, E. Mincione and P. Filippone, Tetrahedron, 2002, 58, 8493–8500.